

Article

Dual Resonant Frequency Inductive Power Transfer in an Underwater Tight Coupling System

Jing Zhou ¹, Pengzhi Yao ¹, Rui He ¹, Kan Guo ¹, Yao Zhang ^{2,*} and Hao Ma ¹

¹ College of Electrical Engineering, University of Zhejiang, Hangzhou 310027, China; jingzhou@zju.edu.cn (J.Z.); japraul@126.com (P.Y.); ruihe_hurry@zju.edu.cn (R.H.); 21710092@zju.edu.cn (K.G.); mahao@zju.edu.cn (H.M.)

² School of Automation, University of Hangzhou Dianzi, Hangzhou 310000, China

* Correspondence: yaozhang@hdu.edu.cn; Tel.: +86-1876-716-9085

Abstract: The application of wireless power transfer technology in the underwater environment proposes both opportunities and challenges to undersea power feeding. Due to the attenuation of electromagnetic waves in seawater, the distance between transmitter and receiver is always maintained at a minimum value, which results in tight coupling between the transmitter and receiver. The tight coupling condition provides a low impedance loop for high-order harmonic, so the component of the harmonic wave is thus significantly increased and cannot be ignored in the power transmission system. In order to fully utilize the harmonic energy, a fundamental-harmonic dual-channel system was proposed and studied in this paper. Compared with single-channel systems transmitting fundamental wave only, the dual-channel system has higher power transmission capability, while the loss in dual channel system can be less than that of a single-channel system after proper optimization. A 3 kW experiment platform is established to verify the effectiveness of theoretical analysis.

Keywords: inductive power transfer; resonant; harmonic; tight coupling



Citation: Zhou, J.; Yao, P.; He, R.; Guo, K.; Zhang, Y.; Ma, H. Dual Resonant Frequency Inductive Power Transfer in an Underwater Tight Coupling System. *Energies* **2021**, *14*, 242. <https://doi.org/10.3390/en14010242>

Received: 27 November 2020

Accepted: 29 December 2020

Published: 5 January 2021

Publisher's Note: MDPI stays neutral with regard to jurisdictional claims in published maps and institutional affiliations.



Copyright: © 2021 by the authors. Licensee MDPI, Basel, Switzerland. This article is an open access article distributed under the terms and conditions of the Creative Commons Attribution (CC BY) license (<https://creativecommons.org/licenses/by/4.0/>).

1. Introduction

The development of underwater robotics is an important field of research and a promising industrial application since it represents a sustainable solution to exploit ocean resources with a reasonable environmental impact [1]. The application of wireless power transfer technology to underwater devices [2–4] has potential technical and economic benefits, compared to the wet plug technology, which is complicated to implement and expensive to maintain (shown in Figure 1). Wireless power transfer facilitates electrical isolation between the transmitter and receiver and eliminates the compulsory physical contact from power feeder to consumer [5–7]. However, currently, the majority of research mainly focuses on wireless power transfer in the atmospheric environments [8,9], the application in the undersea environment raised new challenges to the development of the WPT (wireless power transfer) technology. On one hand, the conductivity of air at standard temperature and pressure is nearly zero, so the medium loss is not incorporated in the analysis of the theoretical model. The eddy current loss in seawater cannot be ignored, and it has a significant influence on the system efficiency at high operation frequency. On the other hand, wireless power transfer requires a stable alignment of the transmitter and receiver; however, the electromagnetic coupler in seawater is vulnerable to ocean current disturbance, additional mechanical fixing design is required.

Due to the attenuation of electromagnetic wave in seawater [10–12], the distance between transmitter and receiver is maintained at a minimum value, which results in tight coupling between the transmitter and receiver (the coupling coefficient is greater than 0.5), so the underwater inductive power transfer system is a strong coupling system [13–17]. The component of the harmonic wave is thus significantly increased [18–20] and cannot be

ignored in the power transmission system. This paper proposes a dual resonant frequency inductive power transfer system, in which the fundamental and third harmonic waves are transferred simultaneously. The multi-frequency WPT for smart power distribution among multi-standard receivers has been investigated in [21]. A GaN (Gallium nitride)-based programmable pulse width modulation [22] and a concurrent transmitter consisting of two independent transmitters [23] were proposed and implemented to support the dual-mode WPT operation. A scheme that amplifies both the fundamental and third harmonic generated by a full-bridge inverter was proposed to implement the double-frequency WPT (DF-WPT) [24]. A multi-frequency superposition methodology [25] and a multi-frequency drive configuration [26] have been proposed to achieve high efficiency and flexible power distribution for multi-load WPT. In order to reduce the effect of electromagnetic interference, snubbers for power switch devices are necessary, and their effectiveness has been verified in previous literature [27].

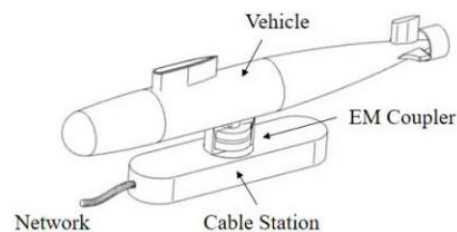


Figure 1. Underwater wireless power transfer system.

In this paper, the compensation network on the primary side is designed with LC stepped structure featuring multiple resonant frequencies. The dual-channel wireless power transfer system is compared with the single-channel system in power losses, including winding loss and circuit loss. Theoretical analysis is validated through simulation and experimental results.

2. Dual Resonant Frequency Inductive Power Transfer

This section starts with the analysis in a mutual inductance model transmitting only a fundamental wave, and an additional circuit branch is added to build the fundamental-harmonic dual-path topology. As extra rectifier bridge and coils were used, the dual channel system transmitting both fundamental and harmonic wave was analyzed and compared with single-channel WPT system in system losses.

2.1. Dual Channel Inductive Power Transfer

The single-channel S-S (series to series) compensated wireless power transfer system is shown in Figure 2.

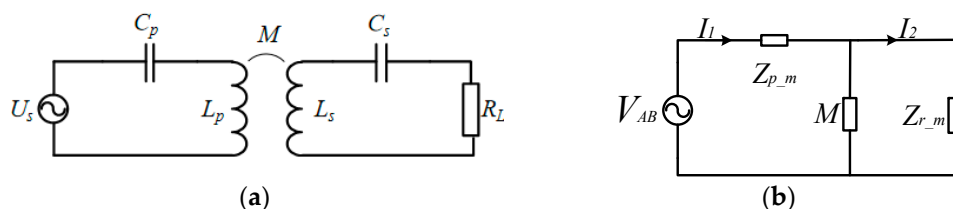


Figure 2. Mutual inductance model: (a) S-S compensated wireless power transfer system, (b) impedance model of S-S compensated WPT system.

Through the Fourier decomposition of the Inverter output square wave voltage,

$$v_{AB} = \frac{4U_s}{\pi} \sum_{m=1,3,5,\dots} \frac{1}{m} \sin(m\omega t) \quad (1)$$

ω is the switching angle frequency.

Subscript m is defined as the circuit parameter in m -th harmonic.

The impedances on the primary and secondary sides are:

$$Z_{p_m} = j(m\omega)L_p + \frac{1}{j(m\omega)C_p} \quad (2)$$

$$Z_{s_m} = j(m\omega)L_s + \frac{1}{j(m\omega)C_s} + R_L \quad (3)$$

The reflected impedance of Z_{R_m} on the primary side is:

$$Z_{R_m} = \frac{[(m\omega)M]^2}{Z_{s_m}} \quad (4)$$

The total input impedance on the primary side is:

$$Z_{in_m} = Z_{p_m} + Z_{R_m} \quad (5)$$

At resonant frequency f_r , the fundamental input impedance is:

$$Z_{in_r} = \frac{\omega_r^2 M^2}{R_L} \quad (6)$$

The quality factor of secondary coil Q_s is defined as:

$$Q_s = \frac{\omega_r L_s}{R_L} \quad (7)$$

The normalized input impedance Z_{inN_m} is:

$$Z_{inN_m} = j \frac{m^2 - 1}{m Q_s} \frac{1}{k^2} + \frac{m^3}{m + j Q_s (m^2 - 1)} \quad (8)$$

The normalized input harmonic current is:

$$I_{PN_m} = \frac{I_{s_m}}{I_{s_r}} = \frac{U_{s_m} / |Z_{in_m}|}{U_{s_r} / |Z_{in_r}|} = \frac{1}{m |Z_{in_mN}|} = \frac{1}{m \left| j \frac{m^2 - 1}{m Q_s} \frac{1}{k^2} + \frac{m^3}{m + j Q_s (m^2 - 1)} \right|} \quad (9)$$

I_{s_m} is the total input current on the primary side, and I_{s_r} is the fundamental input current at resonant frequency f_r .

Under different quality factors, the variation of the third harmonic component with the coupling coefficient is shown in Figure 3. With the increase of the coupling coefficient, the third harmonic component increases first before decreasing. When the transmitter and receiver coils are under tight coupling condition, the component of third harmonic cannot be neglected.

In an underwater WPT system, the gap between the transmitter and receiver coil is tiny, which results in a high coupling coefficient, and the harmonic component is significantly increased.

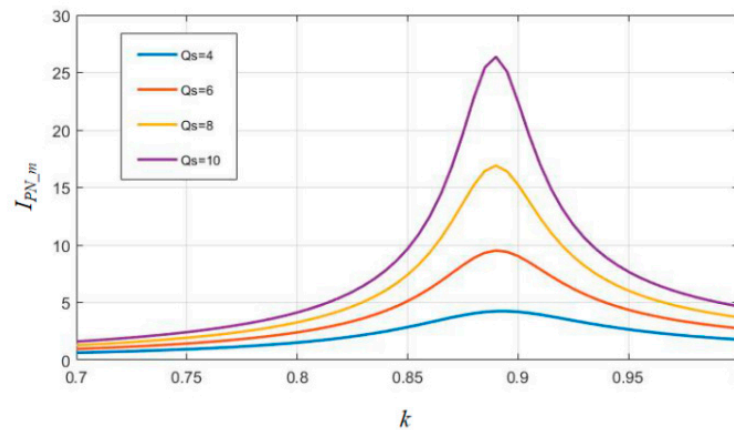


Figure 3. Component of the third harmonic with variation of coupling coefficient.

In order to transfer the fundamental and harmonic wave simultaneously, an additional circuit is usually added to transfer the harmonic wave. A schematic diagram of the fundamental-harmonic dual-path topology is shown in Figure 4. The fundamental and harmonic compensation network is designed at its respective resonant frequency. The two networks share the same inverter bridge. However, this strategy requires two compensation networks and two couplers, which significantly increase the cost and volume of the system; meanwhile, the two outputs will affect the original input angle, and the inverter no longer works under the ZVS (zero voltage switching) condition.

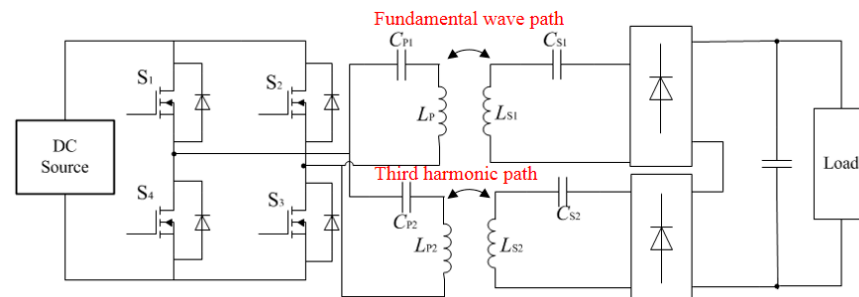


Figure 4. Fundamental-harmonic dual-path wireless power transfer.

As a result, in order to transfer the fundamental and harmonic wave simultaneously, the primary compensation network needs to have multiple resonant frequencies, as shown in Figure 5. Resistor–capacitor–diode clamp snubber was added to the inverter to reduce electromagnetic interference. Multiple resonant frequency network usually employs the LC stepped structure, and the combination of multiple resonant networks enables the system to have multiple resonant frequencies, due to the frequency-selective characteristic of a single LC network. X_e is a reactance unit used to control the phase. The secondary side employs multiple output circuits, to transfer the fundamental and third harmonic wave independently. As the proposed system topology features constant voltage output, the rectifier bridge outputs can be connected in series.

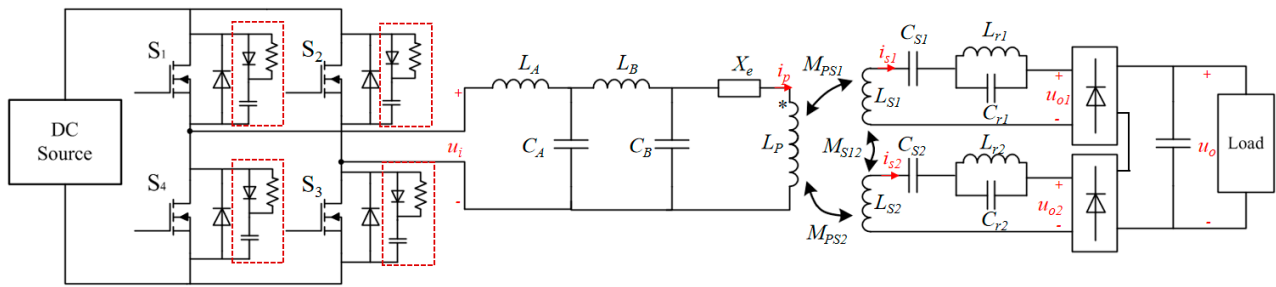


Figure 5. Dual-resonant-frequency wireless power transfer system.

The additional passive compensation network is added on the receiver side (L_{r1} and C_{r1} , L_{r2} and C_{r2}) to eliminate the effects of cross-coupling. As Channel 1 (L_{s1} and C_{s1}) is designed to transfer the fundamental wave and Channel 2 (L_{s2} and C_{s2}) is designed to transfer only the third harmonic, L_{r1} and C_{r1} are designed to be resonant at the third harmonic frequency, and L_{r2} and C_{r2} are designed to be resonant at the fundamental frequency. For Channel 1, the impedance of the third harmonic is infinite, so the third harmonic can hardly go through Channel 1. Similarly, a fundamental wave can hardly go through Channel 2.

2.1.1. Determination of Circuit Parameters

As to the LCL compensation network (shown in Figure 6a, L_A resonant with C_A ensures constant current output, and when L_A equals L_B , the input impedance is resistive). The LCL compensation network is a third-order system with a single resonant frequency. A dual resonant frequency system can be obtained by adding C_B after L_B , as shown in Figure 6b.

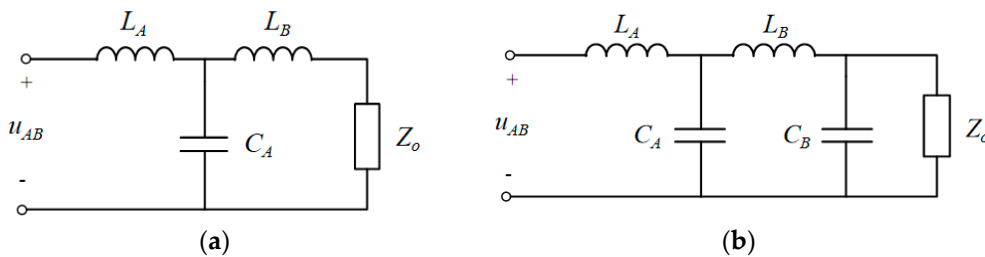


Figure 6. Compensation networks: (a) LCL, (b) dual resonant frequency network.

Define s_ω as negative frequency, $s_{\omega_m} = j\omega_m$

The current gain of dual resonant frequency network G_{iP} is:

$$G_{iP} = \frac{I_P}{U_{AB}} = \frac{1}{s_\omega^4 L_A L_B C_A + s_\omega(L_A + L_B) + [s_\omega^4 L_A L_B C_A C_B + s_\omega^2(L_A C_A + L_A C_B + L_B C_B) + 1]Z_o} \quad (10)$$

when $s_\omega^4 L_A L_B C_A C_B + s_\omega^2(L_A C_A + L_A C_B + L_B C_B) + 1 = 0$, G_{iP} is independent of load Z_o . When the system resonant at the fundamental and third harmonic frequency, G_{iP} is independent of load Z_o .

$$\frac{L_A C_A + L_A C_B + L_B C_B}{L_A L_B C_A C_B} = 10\omega_{-1}^2 \quad (11)$$

$$\frac{1}{L_A L_B C_A C_B} = \frac{1}{9}\omega_{-3}^4 \quad (12)$$

The current gain is:

$$G_{iP}(\omega_{-1}) = G_{iP}(\omega_{-3}) = \frac{1}{s_{\omega}^3 L_A L_B C_A + s_{\omega} (L_A + L_B)} \quad (13)$$

The current gains for fundamental and third harmonic are defined as G_{-1} and G_{-3} , respectively:

$$G_{-1} = \frac{1}{L_A L_B C_A \omega_{-1}^3 - (L_A + L_B) \omega_{-1}} \quad (14)$$

$$G_{-3} = \frac{1}{L_A L_B C_A \omega_{-3}^3 - (L_A + L_B) \omega_{-3}} \quad (15)$$

Solving the equations,

$$\begin{cases} L_A = \frac{1}{3\omega_{-1}(G_{-3}-3G_{-1})} \\ L_B = \frac{(G_{-1}-3G_{-3})^2}{8\omega_{-1}G_{-1}G_{-3}(3G_{-1}-G_{-3})} \end{cases} \quad (16)$$

$$\begin{cases} C_A = \frac{(3G_{-1}-G_{-3})^2}{8\omega_{-1}(3G_{-3}-G_{-1})} \\ C_B = \frac{8G_{-1}G_{-3}}{3\omega_{-1}(G_{-1}-3G_{-3})} \end{cases} \quad (17)$$

Therefore, given the current gains G_{-1} and G_{-3} and fundamental frequency, the values of L_A , L_B , C_A , and C_B can be determined.

2.1.2. System Output Characteristics

The constant voltage output condition is:

$$\begin{cases} \omega_1 L_{s1} - \frac{1}{\omega_1 C_{s1}} + \frac{\omega_1 L_{r1}}{1 - \omega_1^2 L_{r1} C_{r1}} = 0 \\ \omega_3 L_{s2} - \frac{1}{\omega_3 C_{s2}} + \frac{\omega_3 L_{r2}}{1 - \omega_3^2 L_{r2} C_{r2}} = 0 \end{cases} \quad (18)$$

The two receiver circuits are decoupled under the condition:

$$\begin{cases} 1 - \omega_3^2 L_{r1} C_{r1} = 0 \\ 1 - \omega_1^2 L_{r2} C_{r2} = 0 \end{cases} \quad (19)$$

The AC voltage gain is:

$$\begin{cases} G_{v1} = \left| \frac{U_{o1}}{U_{i1}} \right| = \left| \frac{\omega_1 M_{PS1} I_{P1}}{U_{i1}} \right| = \omega_1 M_{PS1} |G_{iP1}| \\ G_{v2} = \left| \frac{U_{o2}}{U_{i3}} \right| = \left| \frac{\omega_3 M_{PS2} I_{P3}}{U_{i3}} \right| = \omega_3 M_{PS2} |G_{iP3}| \end{cases} \quad (20)$$

As the rectifier bridge outputs connect in parallel,

$$U_o = \frac{\pi}{4} (U_{o1} + U_{o2}) \quad (21)$$

The power in each receiver circuit is distributed according to the ratio of voltage distribution,

$$\begin{cases} P_{o1} = \frac{U_{o1}}{U_o} \cdot \frac{U_o^2}{R_L} = \frac{U_{o1} U_o}{R_L} \\ P_{o2} = \frac{U_{o2}}{U_o} \cdot \frac{U_o^2}{R_L} = \frac{U_{o2} U_o}{R_L} \end{cases} \quad (22)$$

If the rectifier bridge loss is neglected, the power flows in the rectifier equals the power flows out,

$$\begin{cases} U_{o1}I_{s1} = P_{o1} = \frac{U_{o1}U_o}{R_L} = I_oI_{o1}R_L \\ U_{o2}I_{s2} = P_{o2} = \frac{U_{o2}U_o}{R_L} = I_oI_{o2}R_L \end{cases} \quad (23)$$

Therefore, the equivalent resistances with the rectification of two receiver circuits are:

$$\begin{cases} R_{E1} = \frac{U_{o1}}{I_{s1}} = \frac{16}{\pi^2}R_L \frac{|M_{PS1}G_{iP1}|}{|M_{PS1}G_{iP1}|+|M_{PS2}G_{iP3}|} \\ R_{E2} = \frac{U_{o2}}{I_{s2}} = \frac{16}{\pi^2}R_L \frac{|M_{PS2}G_{iP3}|}{|M_{PS1}G_{iP1}|+|M_{PS2}G_{iP3}|} \end{cases} \quad (24)$$

2.2. Comparison of Dual and Single Channel Systems

The comparison of dual- and single-channel systems is carried out in terms of inverter circuit conduction loss and winding loss in a loosely coupled transformer.

The total power output of the system is P_o , the power output of receiver circuit 1 is P_{o1} , and the power output of receiver circuit 1 is P_{o2} .

To define power factor λ , the equivalent load resistance of the single-channel system is:

$$\begin{cases} \lambda = \frac{P_{o1}}{P_o} = \frac{|M_{PS1}G_{iP1}|}{|M_{PS1}G_{iP1}|+|M_{PS2}G_{iP3}|} \\ 1 - \lambda = \frac{P_{o2}}{P_o} = \frac{|M_{PS2}G_{iP3}|}{|M_{PS1}G_{iP1}|+|M_{PS2}G_{iP3}|} \end{cases} \quad (25)$$

Assuming the current gain of the single-channel system is G_{iP} , the total power output in the single-channel system is:

$$R_E = \frac{8R_L}{\pi^2} \quad (26)$$

$$P_o = \frac{|\omega_1 M_{PS1} U_{i1} G_{iP}|^2}{R_E} \quad (27)$$

while the power outputs in the dual-channel system are:

$$\begin{cases} P_{o1} = \frac{|\omega_1 M_{PS1} U_{i1} G_{iP1}|^2}{R_{E1}} \\ P_{o2} = \frac{|\omega_3 M_{PS2} U_{i3} G_{iP3}|^2}{R_{E2}} \end{cases} \quad (28)$$

Defining $\delta = M_{PS1}/M_{PS2}$, solving (17)–(20), and normalizing current gain G_{iP1} , G_{iP3} and equivalent resistance R_{E1} and R_{E2} :

$$\begin{cases} G_{iP1_N} = \frac{G_{iP1}}{G_{iP}} = \sqrt{2}\lambda, G_{iP3_N} = \frac{G_{iP3}}{G_{iP}} = \sqrt{2}\delta(1 - \lambda) \\ R_{E1_N} = \frac{R_{E1}}{R_E} = 2\lambda, R_{E2_N} = \frac{R_{E2}}{R_E} = 2(1 - \lambda) \end{cases} \quad (29)$$

2.2.1. Rectifier Circuit Conduction Loss

Assume there is no loss in passive elements, the output power from the inverter equals the input power to the rectifier, and the input current on the primary side is as follows:

Single channel:

$$I_{in} = \frac{|\omega_1 M_{PS1} G_{iP}|^2}{R_E} U_{in} \quad (30)$$

Dual channel:

$$\begin{cases} I_{in1} = \frac{|\omega_1 M_{PS1} G_{iP1}|^2}{R_{E1}} \cdot U_{in1} \\ I_{in3} = \frac{|\omega_3 M_{PS2} G_{iP3}|^2}{R_{E2}} \cdot U_{in3} \end{cases} \quad (31)$$

The normalized input current expression is:

$$I_{in_N} = \frac{\sqrt{I_{in1}^2 + I_{in3}^2}}{I_{in}} = \sqrt{\lambda^2 + 9(1 - \lambda)^2} \quad (32)$$

The normalized input current curve of the dual-channel system is plotted in Figure 7. When the power factor λ is greater than 0.8, the input current in the dual-channel system is smaller than the single-channel system, and when $\lambda = 0.9$, the normalized current achieves its minimum value of 0.9. As the input current into the resonant network is the break-over current in the inverter circuit. As a result, to maintain a low conduction loss, the dual-channel system should be designed to work in the shaded region shown in Figure 7.

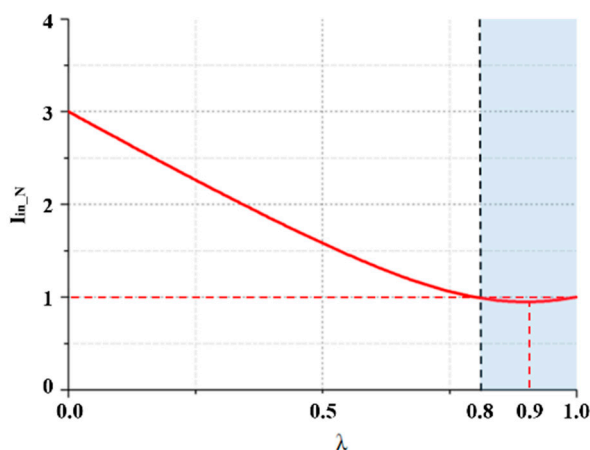


Figure 7. Normalized dual-channel input current.

2.2.2. Winding Loss on Loosely Coupled Transformer

The fundamental and third harmonic current on the primary side is:

$$\begin{cases} i_{p1} = U_{in1}|G_{iP1}|\sin(\omega_1 t + \varphi_1) \\ i_{p3} = U_{in3}|G_{iP3}|\sin(3\omega_3 t + \varphi_3) \end{cases} \quad (33)$$

in which, φ_1 is the phase difference between i_{p1} and u_{in1} , and φ_3 is the phase difference between i_{p3} and u_{in3} . As i_{p1} lags behind u_{in1} by 90° , i_{p3} leads u_{in3} by 90° , so i_{p1} and i_{p3} are in-phase. The primary current can be written as:

$$i_p = i_{p1} + i_{p3} = U_{in1}|G_{iP1}|\sin(\omega_1 t) + U_{in3}|G_{iP3}|\sin(3\omega_3 t) \quad (34)$$

Through the derivation with $\omega_1 t$, when

$$\omega_1 t = \arcsin(\sqrt{(|G_{iP1}| + |G_{iP3}|)/4|G_{iP3}|}) \quad (35)$$

i_p achieves its maximum value,

$$I_{p_max} = \frac{U_{in1}(|G_{iP1}| + |G_{iP3}|)}{3} \cdot \sqrt{1 + \left| \frac{G_{iP1}}{G_{iP3}} \right|} \quad (36)$$

Through the derivation with $|G_{iP3}|$, when $|G_{iP3}| = |G_{iP1}|/2$, i_{p_max} achieves its minimum value,

$$\min(i_{p_max}) = \frac{\sqrt{3}}{2} U_{in1} |G_{iP1}| \quad (37)$$

Therefore, the primary current amplitude of the dual-channel system can be reduced to $\sqrt{3}/2$ of the single-channel system, which facilitates the reduction of maximum flux density, so as to reduce EMI.

Define,

$$Q = \frac{\omega_1 M_{PS1}}{R_E}, Q_1 = \frac{\omega_1 M_{PS1}}{R_{E1}}, Q_2 = \frac{\omega_3 M_{PS2}}{R_{E2}} \quad (38)$$

The currents in the secondary coil single system and dual-channel system are as follows:

Single-channel:

$$I_s = Q|G_{ip}|U_{in1} \tag{39}$$

Dual-channel:

$$\begin{cases} I_{s1} = Q_1|G_{ip1}|U_{in1} \\ I_{s2} = Q_2|G_{ip3}|U_{in3} \end{cases} \tag{40}$$

As shown in Figure 8, R_p, R_{s1}, R_{s2} are the equivalent resistance of each coil. The winding loss in single- and dual-channel systems when considering the coil resistance is

$$\begin{cases} P_{Cu_s} = |U_{in1}G_{ip}|^2R_{p1} + |QG_{ip}U_{in1}|^2R_{s1} \\ P_{Cu_D} = |U_{in1}G_{ip1}|^2R_{p1} + |U_{in3}G_{ip3}|^2R_{p3} \\ \quad + |Q_1G_{ip1}U_{in1}|^2R_{s1} + |Q_2G_{ip3}U_{in3}|^2R_{s2} \end{cases} \tag{41}$$

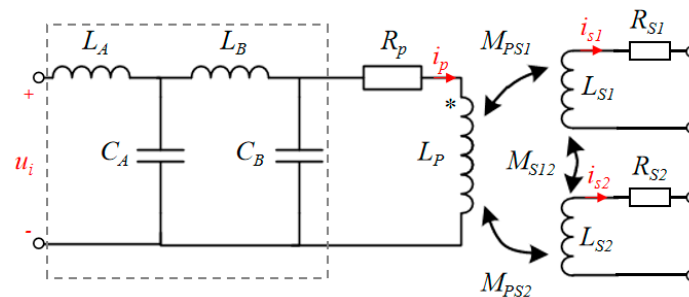


Figure 8. Equivalent circuit of the dual-channel system.

Based on the winding loss in the single-channel system, the winding loss in the dual-channel system is normalized:

$$\begin{aligned} P_{Cu_D_N} &= \frac{P_{Cu_D}}{P_{Cu_s}} \\ &= \frac{18\lambda^2R_{p1} + 2[(1-\lambda)\delta]^2R_{p3} + 4.5Q^2(R_{s1} + R_{s3})}{9(R_{p1} + Q^2R_{s1})} \end{aligned} \tag{42}$$

According to the measured values $R_{p1} = 130 \text{ m}\Omega$, $R_{p3} = 890 \text{ m}\Omega$, $R_{s1} = 120 \text{ m}\Omega$, $R_{s3} = 115 \text{ m}\Omega$, $\delta = 1.88$, the normalized winding loss is plotted in Figure 9 (the trend of the normalized winding loss curve is subject to change according to the variation of internal resistances of coils). In the region below $P_{Cu_D_N} = 1$, the winding loss of the dual-channel system is less than that in the single-channel system.

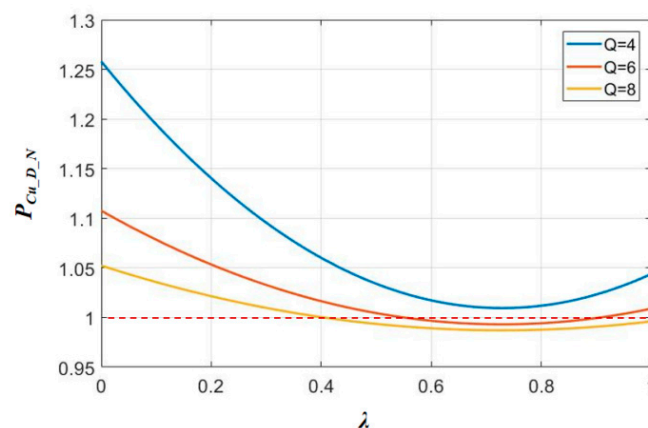


Figure 9. Equivalent circuit of the dual-channel system.

3. Experiment Verification

A 3 kW underwater wireless power transfer (UWPT) platform is established to verify the effectiveness of theoretical analysis. The schematic diagram of the proposed UWPT coupling structure is shown in Figure 10. The side column is designed with an incision angle to increase the contact area and to reduce the magnetic reluctance. Meanwhile, the proposed coupler also has the self-latching function once the transmitter and receiver get to the aligned position, which facilitates its resistance to ocean current disturbance (design and optimization of the coupling structure can be found in [28]). When the underwater vehicle lands on the base station, the receiver is plugged into the transmitter; thus in the charging process, the transmitter and receiver would remain in the fixed position. DMR95 material is utilized as the ferrite core. The gap between transmitter and receiver side varies between 5 and 20 mm, as the waterproof coating is applied on the coupler's surface; the gap of 5 mm is the thickness of the waterproof coating, and the effects of seawater as transmission medium are reduced to a minimum. The couplers are shown in Figure 10. The experimental platform is shown in Figure 11. The experimental setup is shown in Table 1.

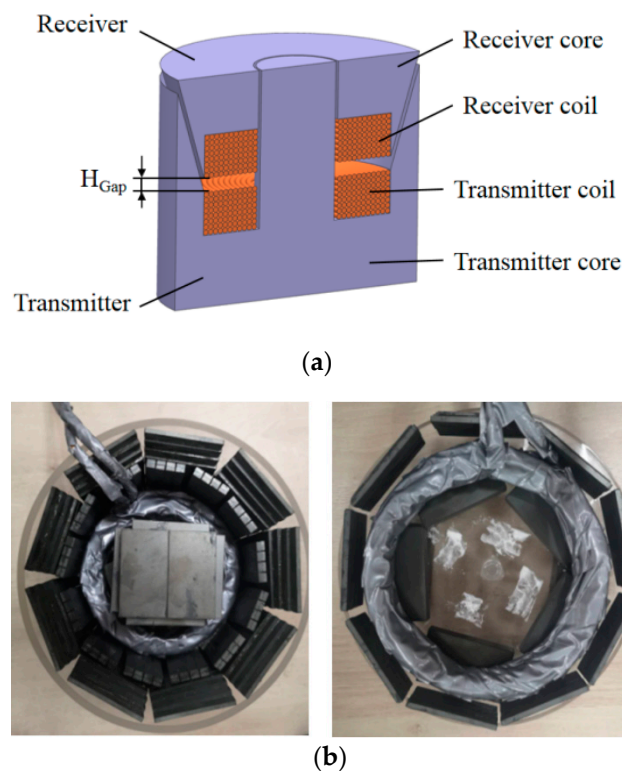


Figure 10. Proposed coupler structure: (a) basic structure; (b) prototype.

Table 1. Component third harmonic as a variation of coupling coefficient.

k	0.52	0.61	0.71	0.82
IP ₃ /IP ₁ (%)	6.72	10.64	22.39	48.56

The influence of the strong coupling condition on system performance was first investigated on a single channel system. When the load resistance is 50 Ω, the inverter output voltage and current waveform are shown and compared in Figure 12. The component of the fundamental wave and third harmonic is then calculated and demonstrated in Table 1. As the coupling coefficient increases from 0.52 to 0.82, the inverter current waveform distortion worsens and the component of third harmonic increases from 6.72% to 48.56%,

which means the component of harmonic increases as the increase of coupling coefficient, which agrees with the theoretical analysis.

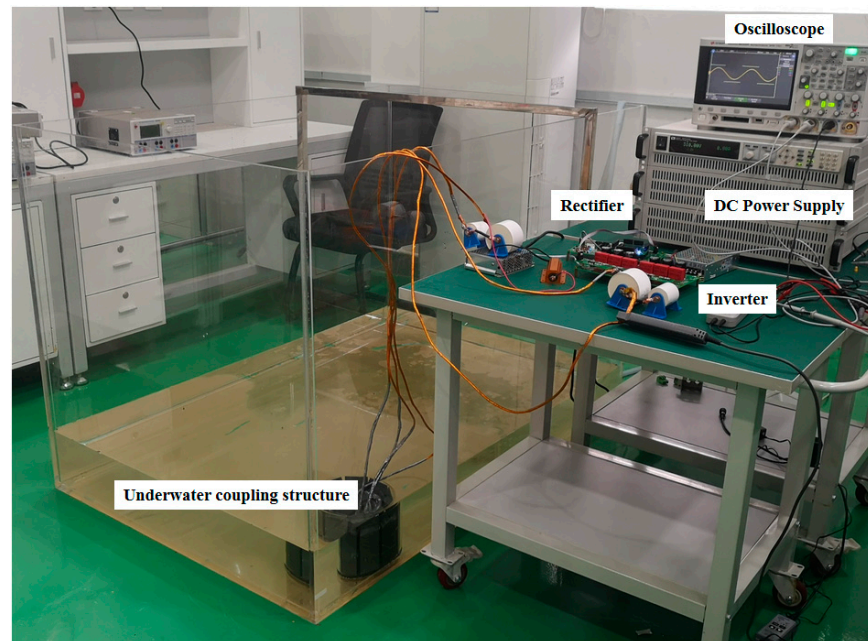


Figure 11. Experiment platform.

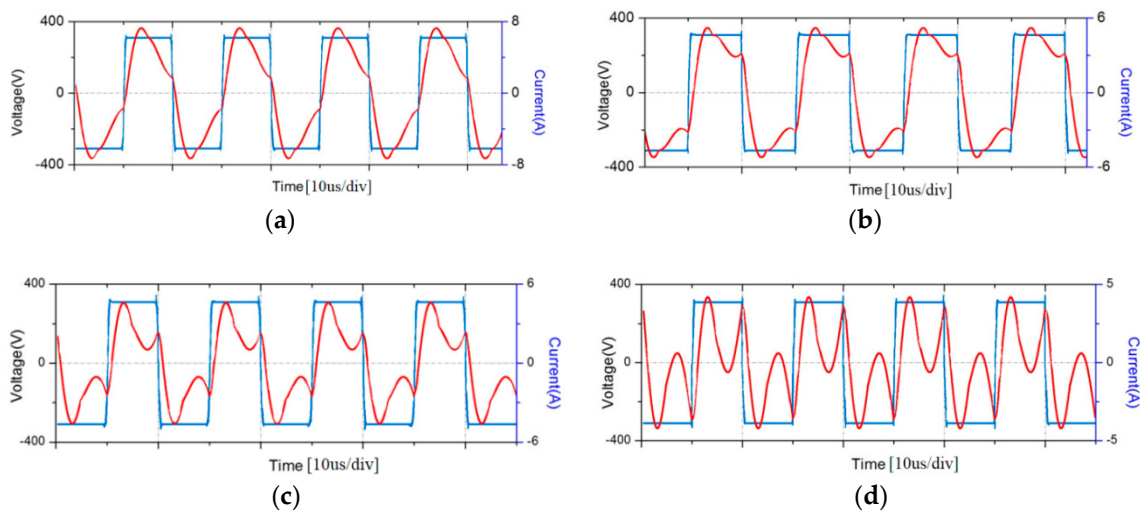


Figure 12. Inverter output voltage and current waveform under different coupling factors: (a) $k = 0.52$; (b) $k = 0.61$; (c) $k = 0.71$; (d) $k = 0.82$.

Based on the single-channel UWPT system, an additional set of coils were added on the receiver side, which shares the same ferrite core with the original coil. The schematic diagram of the fundamental-harmonic dual-path wireless power transfer system is shown in Figure 5. DC power source provides power into the inverter before feeding into the compensation network together with the LC resonant tank. The two receiver coils pick up the power individually, and through the compensation network and rectifier on the receiver side, energy is provided to the load. The output of two receiver networks connects in series. The key parameters of the proposed dual-channel system are shown in Table 2. As few inductance elements were added for dual-frequency resonant network, and the high

work frequency can effectively reduce the inductance volume, independent inductance was utilized.

Table 2. Parameters of the dual-channel system.

Parameters	$L_A/\mu\text{H}$	$L_B/\mu\text{H}$	$L_p/\mu\text{H}$	$L_{s1}/\mu\text{H}$	$L_{s2}/\mu\text{H}$	C_A/nF
Value	106.1	79.6	254.87	252.99	49.01	31.8
Parameters	C_B/nF	C_{s1}/nF	C_{s2}/nF	$L_{r1}/\mu\text{H}$	$L_{r2}/\mu\text{H}$	C_{r1}/nF
Value	42.4	36.8	26.3	20	50	56.3
Parameters	C_{r2}/nF	f/kHz	$M_{ps1}/\mu\text{H}$	$M_{ps2}/\mu\text{H}$	$M_{s12}/\mu\text{H}$	R_L/Ω
Value	202.6	50	200.08	106.41	92.34	50

The key waveform of dual-channel UWPT system is shown in Figure 13. The current in the primary coil is composed of fundamental wave and third harmonic, which proves the dual-frequency resonant characteristic of the transmitter network. The current in Channel 1 (L_{s1} and C_{s1}) only has the fundamental wave, and the current in Channel 2 (L_{s2} and C_{s2}) only has the third harmonic, which proves the frequency-selective characteristic of the receiver compensation network.

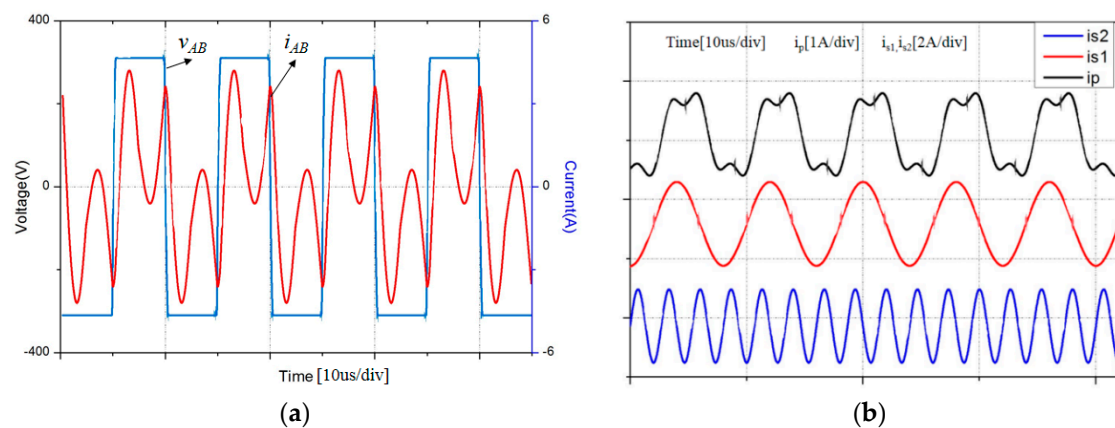


Figure 13. Key waveform of the dual-channel UWPT (under water wireless power transfer) system: (a) inverter output voltage and current; (b) current in primary and secondary coils.

The frequency sweeping curve of system voltage gain is plotted in Figure 14. The crossing point in Channel 1 is right on 50 kHz and the voltage gain is 1.15. Meanwhile, the crossing point in Channel 2 is right on 49.8 kHz and the voltage gain is 0.45. The resonant frequency in Channel 2 is $49.8 \times 3 = 149.4$ kHz. The third harmonic of the inverter output is the input signal into Channel 2.

The maximum power transfer curves of the single- and dual-channel systems are compared in Figure 15, and the dual-channel system's DC-DC efficiency is plotted in Figure 16 and compared with that of the single-channel system (both theoretically and experimentally). For the dual-channel system, the output power equals the output voltage multiplied by output current ($P_O = U_O I_O$). The DC-DC efficiency in this paper is defined as the ratio of output power to input power ($\eta = |U_O I_O / U_{in} I_{in}| \times 100\%$). The dual-channel system possesses higher energy output capability, with higher transmission efficiency. As the load resistance increases, the output power increases first before decreasing. When the output power is 2.69 kW, the system efficiency reaches its maximum value, 92.3%. Utilizing the experimental parameters in equations to calculate total output power and efficiency at specific load conditions $R_L = 30, 40, 50, 60 \Omega$, the theoretical values are plotted and compared with experimental results in Figures 15 and 16.

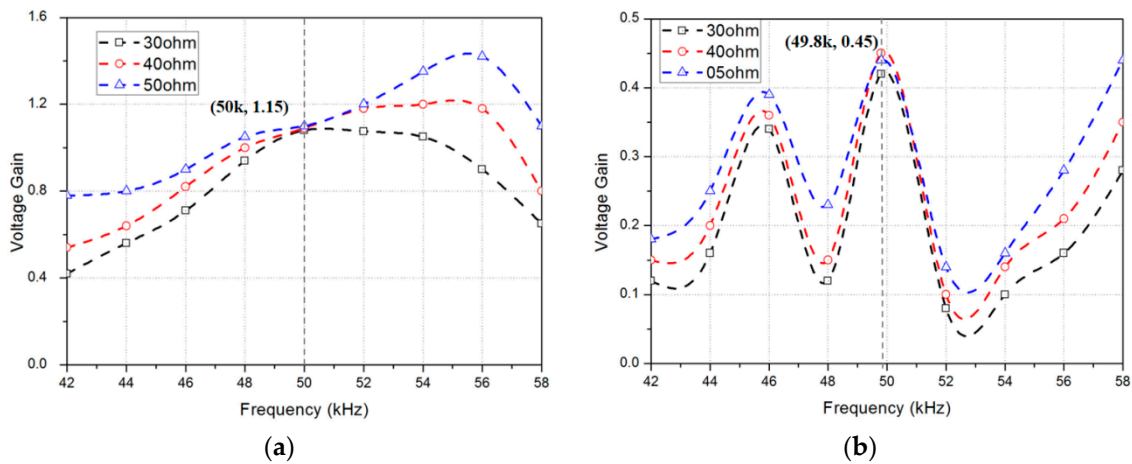


Figure 14. Frequency sweeping curve of system voltage gain in (a) Channel 1; (b) Channel 2.

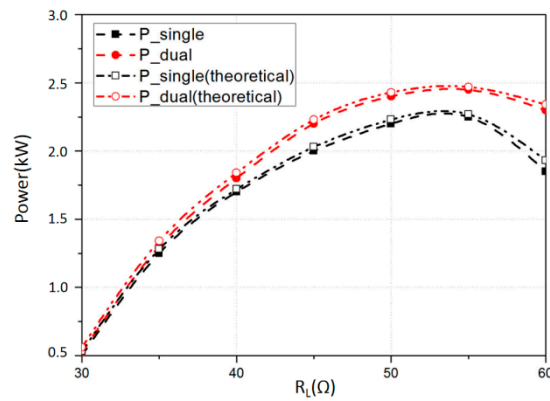


Figure 15. Maximum power transfer curve comparison of the single- and dual-channel systems.

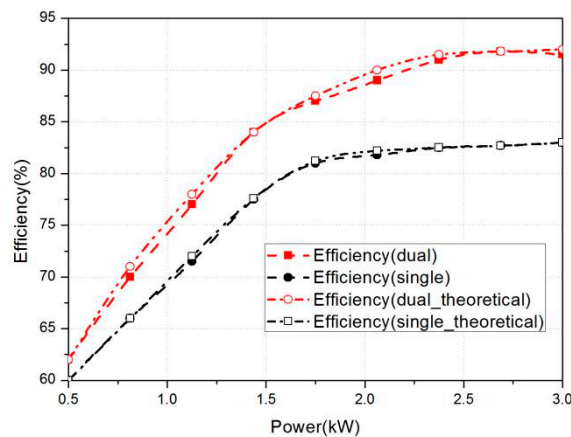


Figure 16. System DC-DC efficiency.

4. Conclusions

For the underwater WPT system, the distance between transmitter and receiver is very small, which results in tight coupling between the transmitter and receiver. The system output characteristics under the tight coupling condition were analyzed based on the calculation of input impedance. The tight coupling condition provided a low impedance loop for high-order harmonic, which significantly increased the component of harmonics in UWPT. In order to fully utilize the harmonic energy, a fundamental-harmonic dual-channel

system was proposed and studied in this paper. An LC stepped structure was applied on the primary side, and the combination of multiple resonant networks enabled the system to have multiple resonant frequencies. An additional LC compensation network was added on the secondary side to decouple the two receiver coils. The power transmission capability of the dual-channel system surpassed that of the single-channel system. The dual-channel system was compared with single-channel system in loss and efficiency. As to the rectifier conduction loss and winding loss, the loss in the dual-channel system was less than that of the single-channel system when the power factor was within a certain range. Theoretical analysis was then validated on a 3 kW underwater wireless power transfer platform. Maximum DC-DC efficiency of 92.3% was achieved. The dual-channel system has a better output characteristic compared with the single-channel system in underwater applications.

Author Contributions: Conceptualization, J.Z. and P.Y.; methodology, J.Z. and P.Y.; validation, J.Z., P.Y. and K.G.; formal analysis, J.Z., R.H. and P.Y.; investigation, K.G.; resources, Y.Z.; writing—original draft preparation, J.Z. and P.Y.; writing—review and editing, J.Z.; supervision, H.M.; project administration, J.Z. All authors have read and agreed to the published version of the manuscript.

Funding: This research was funded by Zhejiang R&D Key Research Plan, grant number 2019C01044 and by Zhejiang Natural Science Foundation, grant number LY18E070004.

Institutional Review Board Statement: Not applicable.

Informed Consent Statement: Not applicable.

Data Availability Statement: Not applicable.

Conflicts of Interest: The authors declare no conflict of interest.

References

1. Benedetto, A.; Luca, P.; Alberto, R.; Fabio, C. Wireless power recharge for underwater robotics. In Proceedings of the 2017 IEEE International Conference on Environment and Electrical Engineering and 2017 IEEE Industrial and Commercial Power Systems Europe (EEEIC/I&CPS Europe), Milan, Italy, 6–9 June 2017; pp. 1–6.
2. Kan, T.; Zhang, Y.; Yan, Z.; Mercier, P.; Mi, C. A Rotation-Resilient Wireless Charging System for Lightweight Autonomous Underwater Vehicles. *IEEE Trans. Veh. Technol.* **2018**, *67*, 6935–6942. [[CrossRef](#)]
3. Kan, T.; Mai, R.; Mercier, P.; Mi, C. Design and analysis of a three phase wireless charging system for lightweight autonomous underwater vehicles. *IEEE Trans. Power Electron.* **2018**, *33*, 6622–6632. [[CrossRef](#)]
4. Lin, M.; Li, D.; Yang, C. Design of an ICPT system for battery charging applied to underwater docking systems. *Ocean Eng.* **2017**, *145*, 373–381. [[CrossRef](#)]
5. Hui, S.Y.R.; Zhong, W.; Lee, C.K. A Critical Review of Recent Progress in Mid-Range Wireless Power Transfer. *IEEE Trans. Power Electron.* **2014**, *29*, 4500–4511. [[CrossRef](#)]
6. Mi, C.C.; Buja, G.; Choi, S.Y.; Rim, C.T. Modern Advances in Wireless Power Transfer Systems for Roadway Powered Electric Vehicles. *IEEE Trans. Industrial Electron.* **2016**, *63*, 6533–6545. [[CrossRef](#)]
7. Zhang, C.; Lin, D.; Tang, N.; Hui, S.Y.R. A Novel Electric Insulation String Structure with High-Voltage Insulation and Wireless Power Transfer Capabilities. *IEEE Trans. Power Electron.* **2018**, *33*, 87–96. [[CrossRef](#)]
8. Zhong, W.X.; Hui, S.Y.R. Maximum Energy Efficiency Tracking for Wireless Power Transfer Systems. *IEEE Trans. Power Electron.* **2015**, *30*, 4025–4034. [[CrossRef](#)]
9. Zhang, C.; Lin, D.; Hui, S.Y.R. Ball-Joint Wireless Power Transfer Systems. *IEEE Trans. Power Electron.* **2018**, *33*, 65–72. [[CrossRef](#)]
10. Zhang, K.; Ma, Y.; Yan, Z.; Di, Z.; Song, B. Eddy Current Loss and Detuning Effect of Seawater on Wireless Power Transfer. *IEEE J. Emerg. Sel. Top. Power Electron.* **2018**, *8*, 909–917. [[CrossRef](#)]
11. Zhang, K.; Zhu, Z.; Du, L.; Song, B. Eddy loss analysis and parameter optimization of the WPT system in seawater. *J. Power Electron.* **2018**, *18*, 778–788.
12. Yan, Z.; Song, B.; Zhang, K.; Wen, H.; Mao, Z.; Hu, Y. Eddy current loss analysis of underwater wireless power transfer systems with misalignments. *AIP Adv.* **2018**, *8*, 101421. [[CrossRef](#)]
13. Zhang, Y.; Kan, T.; Yan, Z.; Mao, Y.; Wu, Z.; Mi, C. Modeling and analysis of series-parallel compensation for wireless power transfer system with a strong coupling. *IEEE Trans. Power Electron.* **2019**, *34*, 1209–1215. [[CrossRef](#)]
14. Jolani, F.; Yu, Y.; Chen, Z. Enhanced planar wireless power transfer using strongly coupled magnetic resonance. *Electron. Lett.* **2015**, *51*, 173–174. [[CrossRef](#)]
15. Ho, S.L.; Wang, J.; Fu, W.N.; Sun, M. A Comparative Study between Novel Witricity and Traditional Inductive Magnetic Coupling in Wireless Charging. *IEEE Trans. Magn.* **2011**, *47*, 1522–1525. [[CrossRef](#)]

16. Zhang, Y.; Yan, Z.; Kan, T.; Liu, Y.; Mi, C.C. Modelling and analysis of the distortion of strongly-coupled wireless power transfer systems with SS and LCC–LCC compensations. *IET Power Electron.* **2019**, *12*, 1321–1328. [[CrossRef](#)]
17. Ahn, D.; Kiani, M.; Ghoyanloo, M. Enhanced Wireless Power Transmission Using Strong Paramagnetic Response. *IEEE Trans. Magn.* **2014**, *50*, 96–103. [[CrossRef](#)]
18. Wang, J.; Ho, S.L.; Fu, W.; Kit, C.T.; Sun, M. Finite-Element Analysis and Corresponding Experiments of Resonant Energy Transfer for Wireless Transmission Devices. *IEEE Trans. Magn.* **2011**, *47*, 1074–1077. [[CrossRef](#)]
19. Sun, T.; Xie, X.; Li, G.; Gu, Y.; Deng, Y.; Wang, Z. A Two-Hop Wireless Power Transfer System with an Efficiency-Enhanced Power Receiver for Motion-Free Capsule Endoscopy Inspection. *IEEE Trans. Biomed. Eng.* **2012**, *59*, 3247–3254.
20. Huh, S.; Ahn, D. Two-Transmitter Wireless Power Transfer with Optimal Activation and Current Selection of Transmitters. *IEEE Trans. Power Electron.* **2018**, *33*, 4957–4967. [[CrossRef](#)]
21. Kim, Y.J.; Ha, D.; Chappell, W.J.; Irazoqui, P.P. Selective wireless power transfer for smart power distribution in a miniature-sized multiple-receiver system. *IEEE Trans. Ind. Electron.* **2016**, *63*, 1853–1862. [[CrossRef](#)]
22. Zhao, C.; Costinett, D. GaN-based dual-mode wireless power transfer using multifrequency programmed pulse width modulation. *IEEE Trans. Ind. Electron.* **2017**, *64*, 9165–9176. [[CrossRef](#)]
23. Ahn, D.; Mercier, P.P. Wireless power transfer with concurrent 200-kHz and 6.78-MHz operation in a single-transmitter device. *IEEE Trans. Ind. Electron.* **2016**, *31*, 5018–5029. [[CrossRef](#)]
24. Pantic, Z.; Lee, K.; Lukic, S.M. Multifrequency inductive power transfer. *IEEE Trans. Power Electron.* **2014**, *29*, 5995–6005. [[CrossRef](#)]
25. Liu, F.; Yang, Y.; Ding, Z.; Chen, X.; Kennel, R.M. A multifrequency superposition methodology to achieve high efficiency and targeted power distribution for a multiload MCR WPT system. *IEEE Trans. Power Electron.* **2018**, *33*, 9005–9016. [[CrossRef](#)]
26. Liu, F.; Yang, Y.; Ding, Z.; Chen, X.; Kennel, R.M. Eliminating cross interference between multiple receivers to achieve targeted power distribution for a multi-frequency multi-load MCR WPT system. *IET Power Electron.* **2018**, *11*, 1321–1328. [[CrossRef](#)]
27. Peng, F.Z.; Su, G.J.; Tolbert, L.M. A Passive Soft-Switching Snubber for PWM Inverters. *IEEE Trans. Power Electron.* **2004**, *19*, 363–370. [[CrossRef](#)]
28. Zhou, J.; Yao, P.; Chen, Y.; Guo, K.; Hu, S.; Sun, H. Design Considerations for a Self-latching Coupling Structure of Inductive Power Transfer for Autonomous Underwater Vehicle. *IEEE Trans. Ind. Appl.* **2020**, *57*, 580–587. [[CrossRef](#)]